UNSTEADY RANS SIMULATION OF THE OFF-DESIGN OPERATION OF A HIGH EXPANSION RATIO ORC TURBINE

Enrico Rinaldi[1], Rene Pecnik[1*], Piero Colonna[2]

[1] Delft University of Technology, Process & Energy Department,
Delft, The Netherlands
e.rinaldi@tudelft.nl, r.pecnik@tudelft.nl

[2] Delft University of Technology, Propulsion and Power,
Delft, The Netherlands
p.colonna@tudelft.nl

* Corresponding Author

ABSTRACT

The design of Organic Rankine cycle (ORC) turbines is a challenging task due to the complex thermodynamic behaviour of the working fluid, the typical high expansion ratio which leads to a highly supersonic flow, and the continuous shift of operation between on- and off-design conditions. Computational fluid dynamic (CFD) simulations provide useful insights on the turbine flow field which help the analysis, design, and optimization process. Steady state CFD computations are becoming nowadays common practice in the design of ORC turbines. However, the inherent unsteadiness of the problem requires time resolved simulations to capture a number of phenomena otherwise ignored, e.g., shock/shock and shock/boundary layer interactions, which are expected to dominate the flow evolution. This paper presents a numerical investigation of the off-design operation of a single stage high expansion ratio (>100) ORC radial turbine. Two-dimensional unsteady Reynolds-averaged Navier-Stokes simulations are presented to highlight the main flow characteristics and to study the stator/rotor interaction in terms of time dependent turbine performance parameters and blade loads. An in-house flow solver was used, which accounts for the non-ideal behaviour of the fluid via look-up tables generated using a multiparameter equation of state model. The documented analysis shows unique insights on the unsteady flow field in a supersonic ORC turbine and represents the first step toward a new component design approach based on non-stationary flow characteristics.

1. INTRODUCTION

Organic Rankine cycle (ORC) turbogenerators are a widely pursued technology for the conversion of external heat sources in the low power range (from few kW_e to few MW_e), such as waste heat from industrial processes or solar radiation. The working principles of an ORC are the same as for a steam Rankine cycle, the only difference being the use of an organic fluid which permits to have moderate cycle maximum pressures, allows for a dry turbine expansion and can be used as a lubricant. It also represents an additional degree of freedom to the designer which can be used to best match the external heat source, therefore making the ORC power system extremely flexible. More details on ORC turbogenerators are given by Colonna et al. (2015).

In terms of turbine design, the use of an organic compound leads to small enthalpy drops and to few stages and low rotational speed machines as a consequence. In the low power range, ORC turbines can reach much higher efficiencies if compared to steam turbines. However, the design

of efficient ORC expanders is a challenging task due to the strongly non-ideal thermophysical behaviour of the fluid, especially in the first stages. In fact, the turbine expansion usually occurs in the fluid dense gas region, whereby the ideal gas law does not hold and real gas effects dominate. Moreover, the typically low speed of sound for an organic fluid often results in supersonic flow conditions for high turbine expansion ratios.

Recently, the use of computational fluid dynamics (CFD) in the design of this non-conventional turbomachinery has gained momentum, as the work of Harinck et al. (2013) and Pasquale et al. (2013) demonstrates showing significant performance improvement of an existing ORC turbine by automated shape optimization of the stator vanes based on steady state CFD computations. Simplified models, as quasi-1D or throughflow calculations, are also common practice and can provide an optimal choice of the main design parameters in the first stages of a machine development, see for example the work of Pini et al. (2013) and Casati et al. (2014).

However, rotating machines present an inherent unsteadiness which becomes more prominent in case of transonic/supersonic flow regimes, as it is the case for ORC turbines. This makes time resolved CFD simulations crucial to represent and study unsteady phenomena otherwise ignored, e.g., shock/shock, shock wave/boundary layer and wake/boundary layer interactions, which affect the turbine operation and performance. Extensive studies were conducted in the past on standard steam and gas turbines. The blades boundary layer evolution and transition under external disturbances was studied by Schulte and Hodson (1998), and the effect on the blade heat load distribution and cooling was analyzed by Michelassi et al. (1999); Teng et al. (2000); Didier et al. (2002). Unsteady blade forces were investigated by Mailach et al. (2004); Rodriguez et al. (2007); Hushmandi et al. (2011). Finally, efficiency increase by vanes clocking in multistage machines was considered by Huber et al. (1996); Griffin et al. (1996); Hummel (2002); Mailach and Vogeler (2004); Schennach et al. (2008).

This paper presents a numerical investigation of the stator/rotor interaction in an ORC high expansion ratio (>100), single stage radial turbine by means of quasi-3D unsteady RANS simulations. Shock/shock and shock/boundary layer interactions are described, and their effect on the blade loads highlighted. An in-house CFD solver is coupled to state-of-the-art thermophysical models to have the highest possible accuracy in the fluid property evaluation. The present work demonstrates the importance of using unsteady simulations to study and design supersonic ORC turbines and provides unique insights on their fluid dynamic operation.

The paper is structured as follows. Sec. 2 presents the turbine geometry and computational grid. The CFD code is briefly described in Sec. 3. Time-averaged pressure distributions on the stator and rotor blades are analyzed in Sec. 4. Sec. 5 presents the time evolution of the turbine flow field and describes unsteady shock/shock and shock/boundary layer interactions. Time dependent rotor blade loads are discussed in Sec. 6. Sec. 7 summarizes the conclusions.

2. TURBINE GEOMETRY

The preliminary design of a single stage, radial inlet turbine operating in a commercial ORC unit is considered in this study. The turbine is made of 18 stator blades and 47 rotor blades. In order to exploit the machine periodicity and to perform CFD simulations on a reduced computational domain, the number of rotor blades was reduced to 45 in the numerical model, so that $\Delta\theta$ = 40 deg only could be modeled. The numerical domain therefore contains 2 stator blades and 5 rotor blades. Figure 1 depicts the real machine and the modeled geometry. The latter was obtained extracting a 2D plane at half the channel height and placing one cell only along the direction perpendicular to the plane. However, the real cross-sectional area variation was maintained as a function of the distance from the axis of rotation, therefore defining a so-called quasi-3D mesh which allows the fluid to expand in a similar manner as it would do in the real 3D geometry. The mesh counts approximately 200,000 hexahedra, which were

Table 1: Turbine boundary conditions. The subscript 0 indicates total conditions and the subscript r denotes reduced quantities, i.e., normalized by the vapour-liquid critical point value.

$T_{0,in}$	$T_{0r,in}$	$P_{0,in}$	$P_{0r,in}$	P_{out}	ω	Walls
314.5 °C	0.99	31.9 bar	0.77	$\nabla P = 0$	24 krpm	Adiabatic

clustered at the walls to ensure that $y^+ \approx 1$. In order to perform CFD simulations, constant total temperature and pressure conditions were set at the inlet of the domain to their design values; a Neumann boundary condition was applied at the supersonic outlet. The stator/rotor sliding interface was treated using a flux-conserving scheme. The solid walls were considered adiabatic. The rotational speed only was set to an off-design value, $\omega = 24,000$ rpm, which is about 8% lower that the design rotational speed, $\omega = 26,000$ rpm. Table 1 summarizes the boundary conditions used for the CFD analysis.

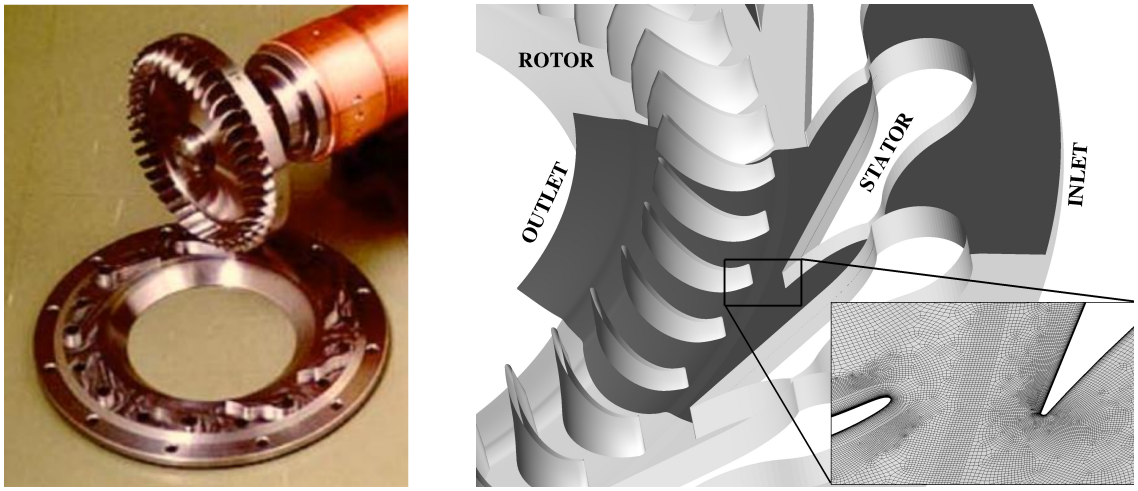

Figure 1: Turbine real geometry (left) and computational domain (right).

3. DENSE GAS CFD SOLVER

A Reynolds-averaged Navier–Stokes solver based on a finite volume formulation on unstructured grids was used. A thorough description of the numerical methods implemented is given by Pecnik et al. (2012b). The one equation turbulence model of Spalart and Allmaras (1994) models the Reynolds stresses. The numerical fluxes and Jacobians are formulated for a general equation of state as described by Rinaldi et al. (2014a). The code was previously validated for applications relevant for this study, see Pecnik et al. (2012a, 2013); Rinaldi et al. (2014b, 2015). Implicit time integration (BDF2) was used to perform the unsteady simulations with a fixed time step chosen such that a period was discretized in 100,000 steps, which lead to a maximum Courant number $CFL \approx 1.5$.

Due to the proximity of the working fluid (Toluene) inlet conditions to its vapour-liquid critical point, the ideal gas model is not applicable. A state-of-the-art multiparameter equation of state model is used instead to model the thermophysical fluid behaviour. Detailed descriptions of the models adopted for thermodynamic and transport properties are given by Olchowy and Sengers (1989); Polt et al. (1992); Lemmon and Span (2006); Santos et al. (2006); Assael et al. (2012). In order to reduce the computational cost of the fluid property evaluation during the CFD simulation, a look-up table built on the above mentioned models is used. A comprehensive analysis of the method is presented by Rinaldi et al. (2014a). The accuracy of the interpolation

on the tabulated thermodynamic area used in this study was verified in a pre-run step. Average and maximum relative errors of the order of 10^{-6} and 10^{-4}, respectively, were calculated for the properties used by the CFD code on a 400x400 nodes table which covers the range ρ_r = $[0.005, 145]$ kg/m^3 and T = $[310, 690]$ K, otherwise expressed in reduced values as ρ = $[1.8 \times 10^{-5}, 0.52]$ and T_r = $[0.52, 1.17]$.

4. TIME-AVERAGED RESULTS

The time-averaged pressure profile along the rotor and stator blades is reported in Fig. 2, together with the maximum and minimum values envelope. The rotor blade profile shows large deviations along the whole blade length as a consequence of the highly unsteady flow evolution in the rotor vanes. On the other hand, the pressure profile in the supersonic part of the stator vane shows no time deviations on Side 1, where the fluid is continuously expanded until the trailing edge of the blade. Small pressure bumps indicate local weak oblique shocks which are a consequence of the thickening of the boundary layer, which changes the wall curvature seen by the flow, and of a possibly low level of smoothness of the surface. Indeed, local differences of the curvature of the surface with respect to the design shape, which was obtained by the method of characteristics, result in compression waves which coalesce into shocks, which can be more clearly observed in Fig. 3. On the opposite side, a similar profile is observed until a shock wave recompresses the fluid at a radial distance from the axis of rotation of about $r \approx 0.123$. At this location, the envelop indicates that the shock impingement position is not fixed but fluctuates. The reason for this oscillations will be highlighted in Sec. 5, where the time evolution of the flow field is described.

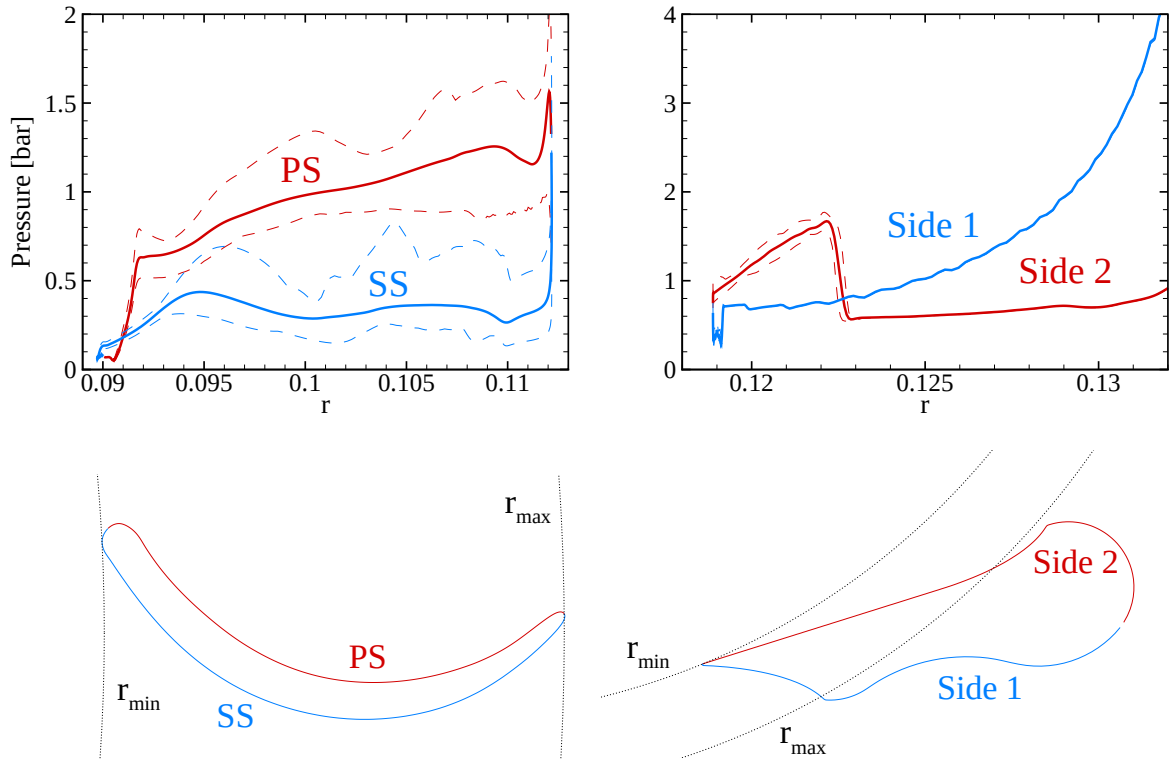

Figure 2: Time-averaged (solid lines), maximum and minimum values (dashed lines) of pressure on the rotor (left) and stator (right) blades. Quantities are functions of the radial distance r from the axis of rotation. LE and TE denote the blade leading edge and trailing edge, respectively.

5. UNSTEADY FLOW EVOLUTION

The evolution of the flow field over a rotor blade passage is studied in this section. Due to the periodicity of the turbine geometry, hereafter we will focus on the passage of one rotor blade, namely blade 0, over one stator vane only. In terms of normalized time $\tau = t/T$, where t denotes the physical time and $T = \Delta\theta/\omega$, this means that the analysis is limited to $\tau = [0, 0.5]$.

Figure 3 displays the pressure gradient magnitude field, by which the strong recompressions induced by the shock waves are easily identifiable. The main flow features are highlighted at $\tau = 0$. The flow is accelerated to sonic conditions in the stator vane throat (TH) and subsequently expands to supersonic conditions in the diverging part of the vane, up to $M \approx 2.8$. Two strong oblique shock waves (ST1 and ST2) are originated from the stator blade trailing edge and recompress the fluid. ST1 directly propagates in the rotor, while ST2 first hits the stator blade wall and then is reflected (R) downstream in the rotor. The rotor flow field shows steady bow shocks (BS) in front of the blunt rotor blades leading edge due to supersonic conditions in the relative frame of reference. BS shocks can be avoided operating the machine at higher rotational speeds. Oblique shock waves (OS) are located on the suction side of the blades and are responsible for large flow separations, largely contributing to the turbine losses, see Fig. 4. Similarly to the stator blade trailing edge, two oblique shocks stem from the rotor blades trailing edge (RT1 and RT2).

At $\tau = 0$, the shock R penetrates the bow shock in front of blade 0 and the oblique shock on the suction side, eventually impinging on the suction side itself in the subsequent time steps. Between $\tau = 2/12$ and $\tau = 4/12$ a similar interaction occurs with ST1. As the blade rotates, BS hits the stator wall near the trailing edge. The shock/boundary layer interaction location moves downstream until the pressure perturbation induced by the shock interacts with the shocks ST1 and ST2, determining their oscillation. This mechanism is responsible for the fluctuation of the reflection point of ST2 into R observed in terms of time-averaged pressure profile in Fig. 2.

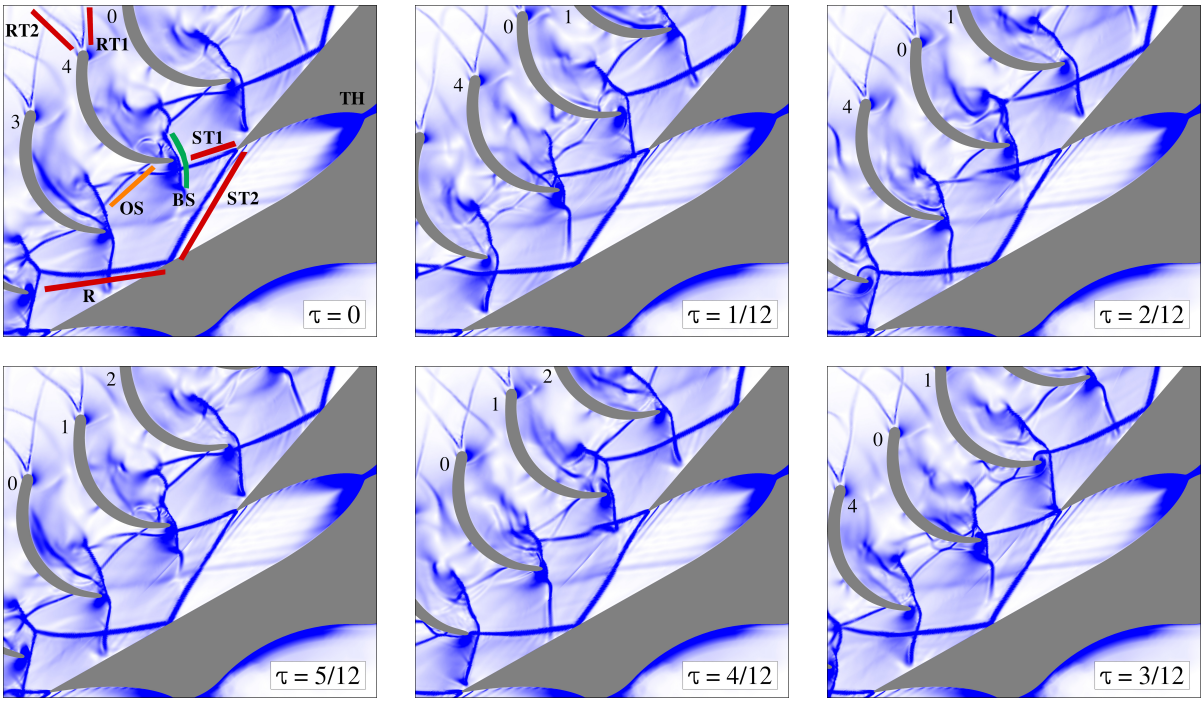

Figure 3: Absolute value of the pressure gradient. The range of values goes from 5 bar/m (white) to 300 bar/m (blue).

The time evolution of the vorticity field is depicted in Fig. 4. A thickening of the boundary layer (black circles, T1 and T2) is observed on the wall of the stator blade and is due to the interaction between the ST2 and BS shocks respectively. As the rotor blades move, T2 follows BS and moves downstream toward the stator blade trailing edge. The wake of the stator blade does not show any vortex shedding, however peaks of vorticity are visible along the wake downstream of the bow shock fronts (dashed lines, SF) The rotor field is dominated by large separation areas (S) on the suction side of the blades, which are induced by the oblique shocks OS depicted in shown in Fig. 3, and which are responsible for most of the losses in the rotor.

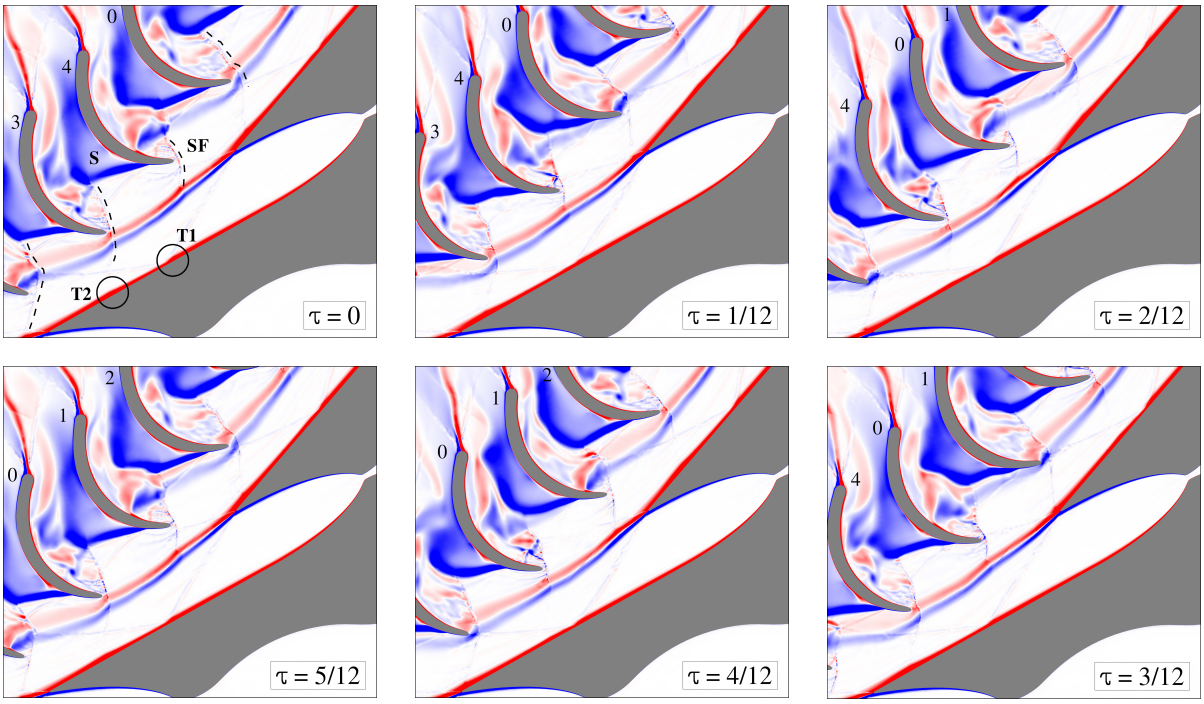

Figure 4: Vorticity field. The range of values goes from -1.5×10^5 1/s (blue) to 1.5×10^5 1/s (red).

6. BLADE LOADS

The rotor blade forces and torque profiles are shown in Fig. 6 for the rotor blade 4 as a function of time over one period. Forces are decomposed on a local frame of reference centered in the center of gravity an aligned with the radial and tangential directions, F_r and F_t respectively, with respect to the center of rotation, see Fig. 5. F_r, F_t and M_z were calculated integrating the pressure over the blade surface. The viscous contribution was neglected since it amounts to $\approx 1\%$ of the pressure's.

Forces and torque profiles show large fluctuations induced by the unsteady shock interactions described in the previous section. The deviation from the time averaged value can be as high as 50% for F_r, 40% for F_t and 90% for M_z.

At $\tau = 0.15$ the tangential component of the force suddenly increases in magnitude due to the detachment of a shock wave from the pressure side of the blade. Therefore, pressure increases along the front part of the pressure side, and as a consequence F_t. This mechanism can be observed in Fig. 3 at $\tau = 2/12$ and $\tau = 2/12$ on the rotor blade 4, and at $\tau = 0$ on blade 3 (the load profiles on the 5 rotor blades only differ by a shift in time by $\tau = 0.2$). A stronger tangential component of the force in the front part of the blade determines a larger (in magnitude) torque, as confirmed by the steep change of M_z at $\tau = 0.15$. The opposite occurs when the tail of the

R shock impinges on the rotor blade suction side at $\tau = 4/12$. Pressure increases locally leading to a drop in the magnitude of F_r and a smaller torque.

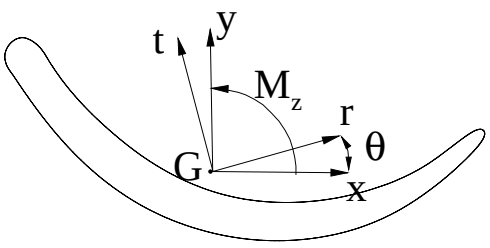

Figure 5: Local frame of reference used to calculate forces and torque on the rotor blades.

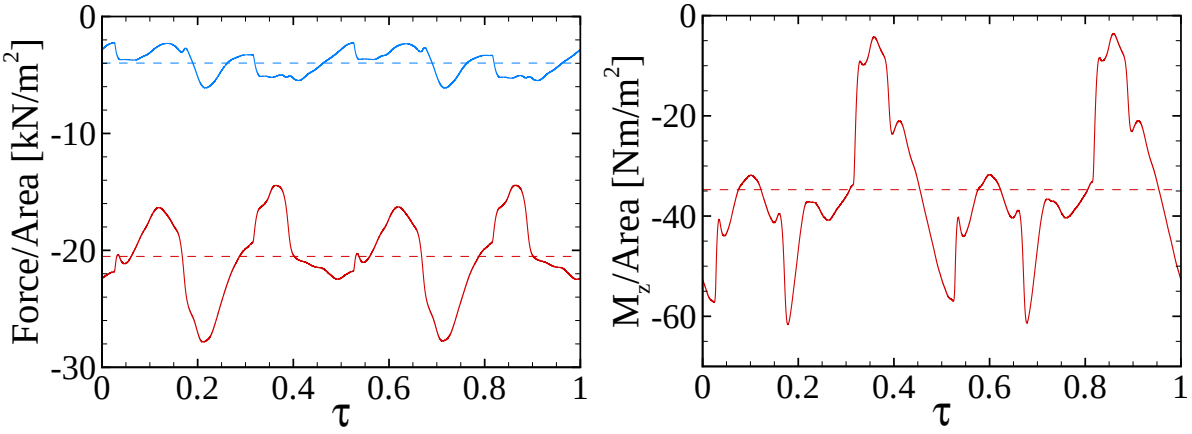

Figure 6: Time evolution of the blade forces and torque. Radial (blue) and tangential (red) components are displayed in the left plot, torque (red) in the right plot. Time-averaged values are also included (dashed lines).

7. CONCLUSIONS

The fluid dynamics of an ORC single stage, high-expansion ratio, radial turbine in off-design conditions was investigated for the first time by means of quasi-3D RANS simulations. An in-house CFD code suited for dense gas flows simulations was used for the study. State-of-the-art thermophysical models were coupled to the CFD code by means of look-up tables, which strongly reduced the computational cost of the fluid property evaluations.

The main interactions between shocks and boundary layers were studied over a time period and identified as the main loss sources the strong trailing edge shocks in the stator, which dynamically interact with the stator blade boundary layer, and the suction side oblique shocks in the rotor, which induce large separation areas. Time-averaged and unsteady rotor blades load profiles were analyzed and showed large forces and torque fluctuations which can be as high as 50% for F_r, 40% for F_t and 90% for M_z. The physical reasons for these sharp load variations were discussed in terms of shock waves interaction with the rotor blades.

The presented study demonstrates the importance of time resolved unsteady CFD simulations

to understand the fluid dynamic operation of supersonic ORC turbines, which are dominated by unsteady flow structures interactions. This investigation highlighted the main loss sources and the fluid dynamic mechanisms responsible for large blade loads fluctuations. This paper represents the first step toward a new ORC turbine design optimization approach based on knowledge and data provided by unsteady CFD simulations.

REFERENCES

Assael, M. J., Mylona, S. K., Huber, M. L., and Perkins, R. A. (2012). Reference correlation of the thermal conductivity of toluene from the triple point to 1000 K and up to 1000 MPa. *J. Phys. Chem. Ref. Data*, 41(2):023101.

Casati, E., Vitale, S., Pini, M., Persico, G., and Colonna, P. (2014). Centrifugal turbines for mini-organic Rankine cycle power systems. *J. Eng. Gas Turb. Power*, 136(12):122607.

Colonna, P., Casati, E., Trapp, C., Mathijssen, T., Larjola, J., Turunen-Saaresti, T., and Uusitalo, A. (2015). Organic Rankine cycle power systems: From the concept to current technology, applications, and an outlook to the future. *Journal of Engineering for Gas Turbines and Power*, 137(10):100801.

Didier, F., Dénos, R., and Arts, T. (2002). Unsteady rotor heat transfer in a transonic turbine stage. *J. Turbomach.*, 124(4):614–622.

Griffin, L., Huber, F., and Sharma, O. (1996). Performance improvement through indexing of turbine airfoils: Part 2 - Numerical simulation. *J. Turbomach.*, 118(4):636–642.

Harinck, J., Pasquale, D., Pecnik, R., van Buijtenen, J., and Colonna, P. (2013). Performance improvement of a radial organic Rankine cycle turbine by means of automated computational fluid dynamic design. *Proc. IMechE, Part A: J. Power and Energy*, 227(6):637–645.

Huber, F., Johnson, P., Sharma, O., Staubach, J., and Gaddis, S. (1996). Performance improvement through indexing of turbine airfoils: Part 1 - Experimental investigation. *J. Turbomach.*, 118(4):630–635.

Hummel, F. (2002). Wake-wake interaction and its potential for clocking in a transonic high-pressure turbine. *J. Turbomach.*, 124(1):69–76.

Hushmandi, N., Fridh, J., and Fransson, T. (2011). Unsteady forces of rotor blades in full and partial admission turbines. *J. Turbomach.*, 133(4).

Lemmon, E. W. and Span, R. (2006). Short fundamental equations of state for 20 industrial fluids. *J. Chem. Eng. Data*, 51(3):785–850.

Mailach, R., Müller, L., and Vogeler, K. (2004). Rotor-stator interactions in a four-stage low-speed axial compressor - Part II: Unsteady aerodynamic forces of rotor and stator blades. *J. Turbomach.*, 126(4):519–526.

Mailach, R. and Vogeler, K. (2004). Rotor-stator interactions in a four-stage low-speed axial compressor - Part I: Unsteady profile pressures and the effect of clocking. *J. Turbomach.*, 126(4):507–518.

Michelassi, V., Martelli, F., Dénos, R., Arts, T., and Sieverding, C. (1999). Unsteady heat transfer in stator-rotor interaction by two-equation turbulence model. *J. Turbomach.*, 121(3):436–447.

Olchowy, G. A. and Sengers, J. V. (1989). A simplified representation for the thermal conductivity of fluids in the critical region. *Int. J. Thermophys.*, 10(2):417–426.

Pasquale, D., Ghidoni, A., and Rebay, S. (2013). Shape optimization of an organic Rankine cycle radial turbine nozzle. *J. Eng. Gas Turb. Power*, 135(4):042308.

Pecnik, R., Rinaldi, E., and Colonna, P. (2012a). Computational fluid dynamics of a radial compressor operating with supercritical CO_2. *J. Eng. Gas Turb. Power*, 134(12):122301.

Pecnik, R., Terrapon, V. E., Ham, F., Iaccarino, G., and Pitsch, H. (2012b). Reynolds-averaged Navier-Stokes simulations of the HyShot II scramjet. *AIAA J.*, 50(8):1717–1732.

Pecnik, R., Witteveen, J. A. S., and Iaccarino, G. (2013). Assessment of uncertainities in modeling of laminar to turbulent transition for transonic flows. *Flow Turbulence Combust.*, 91:41–61.

Pini, M., Persico, G., Casati, E., and Dossena, V. (2013). Preliminary design of a centrifugal turbine for organic Rankine cycle applications. *J. Eng. Gas Turb. Power*, 135(4):042312.

Polt, A., Platzer, B., and Maurer, G. (1992). Parameter der thermischen Zustandsgleichung von Bender fuer 14 mehratomige reine Stoffe. *Chem. Tech.(Leipzig)*, 44(6):216–224.

Rinaldi, E., Pecnik, R., and Colonna, P. (2014a). Exact Jacobians for implicit Navier–Stokes simulations of equilibrium real gas flows. *J. Comput. Phys.*, 270:459–477.

Rinaldi, E., Pecnik, R., and Colonna, P. (2015). Computational fluid dynamic simulation of a supercritical CO_2 compressor performance map. *J. Eng. Gas Turb. Power*, 137(7):072602.

Rinaldi, E., Suarez Raspopov, R., Colonna, P., and Pecnik, R. (2014b). Modeling curvature effects on turbulence transition for turbomachinery flows. In *Proceedings of the ASME Turbo Expo*, pages 1–11.

Rodriguez, C., Egusquiza, E., and Santos, I. (2007). Frequencies in the vibration induced by the rotor stator interaction in a centrifugal pump turbine. *J. Fluid. Eng.-T. ASME*, 129(11):1428–1435.

Santos, F. J. V., Nieto De Castro, C. A., Dymond, J. H., Dalaouti, N. K., Assael, M. J., and Nagashima, A. (2006). Standard reference data for the viscosity of toluene. *J. Phys. Chem. Ref. Data*, 35(1):1–8.

Schennach, O., Pecnik, R., Paradiso, B., Göttlich, E., Marn, A., and Woisetschläger, J. (2008). The effect of vane clocking on the unsteady flow field in a one-and-a-half stage transonic turbine. *J. Turbomach.*, 130(3):031022.

Schulte, V. and Hodson, H. (1998). Unsteady wake-induced boundary layer transition in high lift LP turbines. *J. Turbomach.*, 120(1):28–35.

Spalart, P. R. and Allmaras, S. R. (1994). One-equation turbulence model for aerodynamic flows. *Rech. Aerospatiale*, (1):5–21.

Teng, S., Sohn, D., and Han, J.-C. (2000). Unsteady wake effect on film temperature and effectiveness distributions for a gas turbine blade. *J. Turbomach.*, 122(2):340–347.